Title
Characterization of energy response for photon-counting detectors using x-ray fluorescence

Journal
Medical Physics, 41(12)

ISSN
0094-2405

Authors
Ding, Huanjun
Cho, Hyo-Min
Barber, William C
et al.

Publication Date
2014-11-11

DOI
10.1118/1.4900820

Characterization of energy response for photon-counting detectors using x-ray fluorescence

Huanjun Ding and Hyo-Min Cho
Department of Radiological Sciences, University of California, Irvine, California 92697

William C. Barber and Jan S. Iwanczyk
DxRay, Inc., Northridgek, California 91324

Sabee Molloi[a)]
Department of Radiological Sciences, University of California, Irvine, California 92697

(Received 13 August 2014; revised 10 October 2014; accepted for publication 15 October 2014; published 11 November 2014)

Purpose: To investigate the feasibility of characterizing a Si strip photon-counting detector using x-ray fluorescence.
Methods: X-ray fluorescence was generated by using a pencil beam from a tungsten anode x-ray tube with 2 mm Al filtration. Spectra were acquired at 90° from the primary beam direction with an energy-resolved photon-counting detector based on an edge illuminated Si strip detector. The distances from the source to target and the target to detector were approximately 19 and 11 cm, respectively. Four different materials, containing silver (Ag), iodine (I), barium (Ba), and gadolinium (Gd), were placed in small plastic containers with a diameter of approximately 0.7 cm for x-ray fluorescence measurements. Linear regression analysis was performed to derive the gain and offset values for the correlation between the measured fluorescence peak center and the known fluorescence energies. The energy resolutions and charge-sharing fractions were also obtained from analytical fittings of the recorded fluorescence spectra. An analytical model, which employed four parameters that can be determined from the fluorescence calibration, was used to estimate the detector response function.
Results: Strong fluorescence signals of all four target materials were recorded with the investigated geometry for the Si strip detector. The average gain and offset of all pixels for detector energy calibration were determined to be 6.95 mV/keV and −66.33 mV, respectively. The detector's energy resolution remained at approximately 2.7 keV for low energies, and increased slightly at 45 keV. The average charge-sharing fraction was estimated to be 36% within the investigated energy range of 20–45 keV. The simulated detector output based on the proposed response function agreed well with the experimental measurement.
Conclusions: The performance of a spectral imaging system using energy-resolved photon-counting detectors is very dependent on the energy calibration of the detector. The proposed x-ray fluorescence technique offers an accurate and efficient way to calibrate the energy response of a photon-counting detector. [http://dx.doi.org/10.1118/1.4900820]

Key words: spectral imaging, photon-counting detector, x-ray fluorescence

1. INTRODUCTION

Recently, there have been substantial advances in energy-resolved photon-counting x-ray detectors, which have shown great potential in medical imaging.[1–8] State of the art photon-counting detectors has a number of advantages compared to the traditional charge-integrating detectors. First, conventional charge-integrating detectors generally work in current mode, which integrates both the signal and noise from the detector and electronics over time. However, unlike quantum noise, electronic noise from the charge-integrating detector contributes to the total image variance as an additional term that does not depend on incident x-ray exposure.[9] Therefore, the presence of electronic noise will substantially reduce the signal-to-noise ratio (SNR) in low-dose imaging when the fraction of electronic noise in the total image variance becomes significant. By using a detection mechanism that is completely different from that of the charge-integrating detectors, photon-counting detectors can eliminate electronic noise, regardless of detector pixel pitch and dose. This mechanism not only reduces the total noise variance in the recorded signal but also offers promising potential for low-dose imaging, where the SNR of the measured images will only be limited by quantum noise. In addition, conventional charge-integrating detectors apply a weighting factor that is proportional to the incident photon energy during the energy conversion process. Thus, low-energy photons, which are preferable for enhancing contrast, are weighted less than high-energy photons, and therefore potentially reducing the overall image

contrast. Photon-counting detectors' energy-resolving capability allows the application of optimal energy weighting functions that are able to improve contrast-to-noise ratio (CNR) for specific imaging tasks.[10–14] Furthermore, the energy discrimination capability of photon-counting detectors allows photons to be sorted according to their energies. Thus spectral data can be acquired within a single exposure with minimal spectral overlap, which improves the efficiency in material decomposition.[8,15–17]

Photon-counting detectors being developed for high flux x-ray imaging typically employ direct conversion sensors based on semiconductors, such as silicon,[4,18–21] cadmium telluride (CdTe),[7,17,22–24] and cadmium-zinc-telluride (CZT).[2,15,25,26] When an incident photon interacts with the semiconductor crystal, electrical charges are generated by photoelectric absorption or Compton scatter. The charges are collected by applying a bias field across the crystal, and then a pulse signal is produced by application specific integrated circuits (ASICs). The pulse height is determined by the amount of charge collection, which is directly proportional to the incident photon energy. Voltage discriminators are used to sort the signal according to the pulse height. In imaging mode, a count will be registered in a counter associated with a given threshold if the pulse height exceeds the predetermined threshold value. In spectroscopy mode, the number of counts as a function of pulse height can be recorded by sweeping the discriminator voltage over the whole energy range.

In order to take advantage of the detector's energy discrimination capability, the recorded pulse height needs to be calibrated against the incident photon energies. Typically, a gain and an offset value will be used to correlate the pulse height with photon energy.[27] The accuracy of the energy calibration will affect the performance of the detector in spectral imaging, where reliable measurement of the photon energies is desired. The recorded pulse height distribution for a monoenergetic incident beam is usually referred to as the detector's energy response function, which is a crucial metric in the estimation of the measured signal from a photon-counting detector.[17] For an ideal photon-counting detector, the detector response function should be expressed by a Gaussian distribution centered at the calibrated incident photon energy with a finite peak width that is determined by the detector energy resolution. However, in reality, the detector response function can be distorted by several artifacts, such as pulse pileup and charge-sharing. At high photon flux, pulse pileup occurs when photons arrive within the dead time of the readout electronics. As a result, the induced pulses will be added and, in most cases, recorded as a single count with a higher energy. On the other hand, charge-sharing, which can be mostly attributed to characteristic x-ray escape, photoelectron range, and charge carrier diffusion, can split the incident photon energy into two or more counts in multiple pixels and with lower energies. Studies have shown that CdTe and CZT photon-counting detectors with a pixel pitch less than 0.5 mm suffer significant penalties in spectral response due to charge-sharing induced by characteristic x-ray escape, when abundant x-rays are present above the k-edge energy of Cd and Te.[28–30] Previous studies have suggested that, although ideal photon-counting detectors offer superior imaging performance compared to conventional charge-integrating detectors, their benefits in dose reduction and material decomposition disappear when the detector response function deteriorates due to high count rate or small pixel pitch.[30,31]

Although the energy response function is an important characteristic of a photon-counting detector, it is extremely challenging to perform an analytical prediction due to the complex nature of the various physical processes.[7,32] In most cases, it is estimated through experimental characterizations using photons with known energies. Conventional calibration techniques generally employ synchrotron sources or radioactive isotopes to produce a monoenergetic spectrum with known photon energy.[17,27] Synchrotron radiation offers an ideal calibration photon source with perfect energy resolution, freely adjustable photon energy, and flux. However, synchrotron radiation is not available in a standard imaging lab and is practically impossible to be used as a routine detector characterization technique. Radioactive isotopes, on the other hand, are more readily available in conventional imaging labs for detector calibration. However, common commercially available isotopes generally have a low activity. In order to achieve a reasonable counting statistics, the calibration process can be very time consuming, especially for large-area detectors with small pixels. Using isotopes with high activity, on the other hand, raises the issues of safety and storage. In addition, radioactive isotopes typically produce multiple characteristic emissions, which make it difficult to evaluate the detector response function. Therefore, there is a need to develop a novel detector characterization technique, which can be readily implemented in a standard imaging lab.

Characteristic emission from a fluorescent target can provide a good source of monoenergetic photon spectra, whose intensity can be easily adjusted through the excitation photon flux and the fluorescent target concentration. Therefore, x-ray fluorescence can be potentially used for detector calibration.[33–37] However, the feasibility of x-ray fluorescence calibration has not been systematically studied. In this paper, we propose to characterize a Si strip photon-counting detector using an x-ray fluorescence technique. Silicon has superior charge carrier mobility and is free of characteristic x-ray escape in the energy range of diagnostic medical imaging. Therefore, small pixel pitch can be used, which not only offers high spatial resolution but also leads to high detector count rate up to a few hundred million counts per second per square millimeter (Mcps/mm^2), which approaches the photon flux in a clinical CT system.[5] With such counting capability, the output count rate linearity of the detector can be significantly improved, leading to a substantial reduction of the pulse pileup effect. However, Si has a relatively small atomic number, which results in low x-ray stopping power. To address this issue, an edge-illumination technique has been used to increase the x-ray attenuation length in the incident direction.[38] It has been suggested that the Si strip detectors can offer high enough quantum efficiency for specific clinical applications, such as breast imaging, where the beam energy is typically low.[1,38] Using the proposed

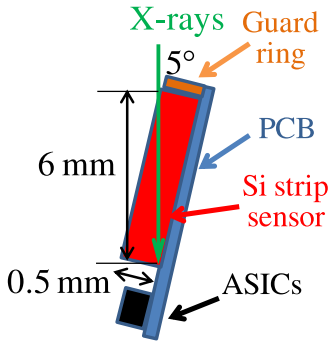

FIG. 1. Schematic of a side view along the Si strip edge-on detector.

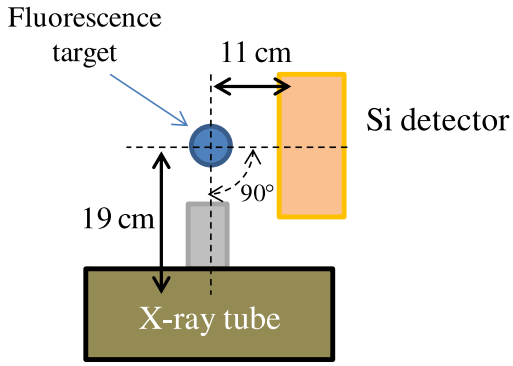

FIG. 2. Experimental setup for the x-ray fluorescence calibration.

x-ray fluorescence technique, we characterized the Si strip detector with four commonly available fluorescent targets: silver (Ag), iodine (I), barium (Ba), and gadolinium (Gd). The recorded fluorescence spectra were used to estimate the pulse height calibration, energy resolution, pixel variation, and charge-sharing fraction of the Si detector. Finally, the detector's energy response function was derived by using an analytical fitting of the experimental results.

2. MATERIALS AND METHODS

2.A. Si strip photon-counting detector

The investigated Si strip photon-counting detector (DxRay, Inc., Northridge, CA) is a small field-of-view (FOV) prototype designed specifically for breast imaging. A schematic drawing of the detector is shown in Fig. 1. It consisted of a single line of 256 pixels with a pixel pitch of 100 μm. The prototype detector is designed using an edge-on geometry with a tilting angle of 5°, so that the incident photon path will not be blocked by the guard rail around the Si sensor. Given the minimal tilting angle and the wafer thickness of 0.5 mm, the effective attenuation length for incident photons was approximately 6 mm. The Si sensor is mounted to a printed circuit board (PCB) that forms a mechanical and electrical substrate thus producing elements that can be tiled in 1D. A bias voltage of 70 V, which is enough to drive the junction into depletion, is applied across the short axis of the Si wafer. One advantage to this design is that the edge illumination provides a small charge collection time, as the charges only travel up to 0.5 mm across the junction regardless of their depth of interaction in the incident direction. This allows for a rapid signal formation required of the fast ASICs designed to produce a high output count rate. The ASICs, which are attached to one side of the PCB, contain charge-sensitive preamplifiers, pulse shaping amplifiers, four pulse height discriminators per pixel, and the associated digital event counters. The threshold levels of all discriminators can be individually fine-tuned through separate 6-bit digital to analog converters (DACs) attached to each discriminator. An offset calibration circuit is designed to calibrate the discriminators to reduce the channel-to-channel variation. The peaking time of the ASIC can be adjusted between 80 and 120 ns.

2.B. X-ray fluorescence measurement setup

The experimental setup for x-ray fluorescence calibration is shown in Fig. 2. A tungsten anode x-ray tube with a focal spot of 0.8 mm was used as the radiation source. The output of the tube was collimated with a cylindrical brass collimator, forming a pencil beam of approximately 1 cm in diameter. An aluminum filter of 2 mm thick was used as prefiltration. The single line Si strip detector was also collimated with a 0.5 mm width brass slit collimator. Using brass instead of lead as the collimating material avoids the contamination from lead fluorescence. Four commonly available fluorescent materials, silver oxide (99%, SIGMA-Aldrich co., MO), iohexol (350 mg/ml iodine, GE Healthcare, Inc., Ireland), barium sulfate (99%, Fisher Scientific, Inc., Waltham, MA), and gadodiamide (287 mg/ml GE Healthcare, Inc., Norway), were used to generate x-ray fluorescence from Ag, I, Ba, and Gd, respectively. The properties of the main fluorescence from these targets are summarized in Table I. The fluorescent materials were placed in small plastic containers with a diameter of approximately 0.7 cm, and the containers were placed approximately 19 and 11 cm away from the x-ray source and the detector, respectively. Experimental data were acquired in a 90° scattering angle as shown in Fig. 2. Fluorescence measurements at higher scattering angles were also made for the iodine target to investigate the angular dependence. However, limited by the physical size of the x-ray tube and the detector, the target to source and the target to detector distances were increased to approximately 31 and 27 cm, respectively. Tube voltages of 70, 80, 90, and 100 kVp were used to excite the fluorescence from the target materials. The tube current was set at 4 mA. The detector's thresholds were scanned from 692 to 20 mV with a frame time of 2.5 s and a step of 4 mV, which corresponds to an approximately 0.57 keV step size

TABLE I. X-ray fluorescence data for the investigated four target materials.

Fluorescent element	Atomic number	k_α (keV)	k_β (keV)	Intensity ratio (k_α/k_β)	k-edge (keV)
Ag	47	22.1	24.9	5.5	25.5
I	53	28.6	32.3	5.3	33.2
Ba	56	32.2	36.4	5.2	37.4
Gd	64	43.0	48.7	5.0	50.2

from 110 to 12 keV. The total recording time for each scan was approximately 7 min. Three scans were acquired and summed for each target materials, so that the measured intensity represents the integrated signal over 7.5 s.

2.C. Data processing

When running in spectroscopy mode, Si strip detector's discriminator threshold scans from high to low pulse height. The signal recorded at each step, which corresponds to the number of pulses whose height exceeds the threshold value of the discriminator is equivalent to the integrated spectra $S_E(t)$. Differentiating the raw data $S_E(t)$ gives the pulse height distribution $P_E(t)$ as a function of discriminator threshold value t. Once the pulse height distribution spectra $P_E(t)$ is recovered, it can be correlated to the incident photon spectra ϕ_E through the detector energy response function DRF(t, E).

$$S_E(t) = \int_0^t P_E(t)dt = \int_0^t \mathrm{DRF}(t, E)\phi_E dt. \quad (1)$$

In the current experimental setup, the detector recorded not only the fluorescence x-ray photons but also the background scatter from the target. Thus, calcium carbonate ($CaCO_3$) powder (Sigma-Aldrich, St. Louis, MO) was first used to estimate the background scattering. Spectra measured with calcium carbonate under the same imaging conditions as that for the fluorescent targets were subtracted from the raw data, which removed the contribution from the background scatter. The resulting signal can then be correlated to the known fluorescence spectra through Eq. (1). An example of the subtracted Ag fluorescence spectra after removing the background scatter is shown in Fig. 3. The primary signals from k-shell fluorescence (k_α and k_β) can be clearly identified. Fluorescence from other shells (L or M) was too weak to be recorded. Due to the detector high counting capability, the pulse pileup effect has been effectively eliminated. This was also evident by the absence of any disenable signals at the energies above the fluorescence peak. However, charge-sharing artifact persists in the recorded spectra, which primarily contributed to the signals at energies below the fluorescence peak.

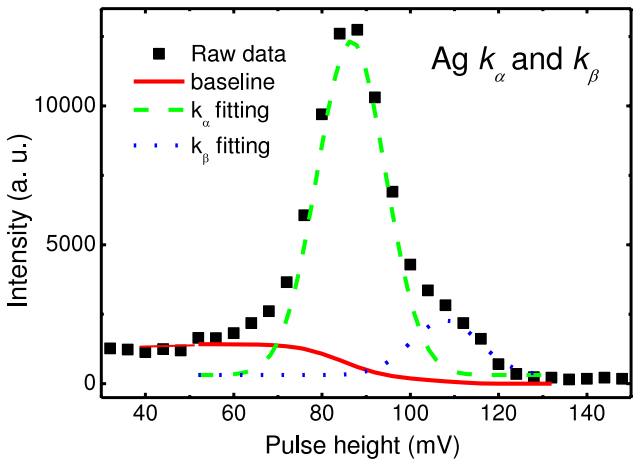

FIG. 3. An example of the recorded Ag fluorescence spectrum with analytical spectrum fitting, including two Gaussian peaks (dash and dot lines) and a baseline function (solid line).

2.C.1. Pulse height calibration

The primary fluorescence signals in the recorded spectra were fitted with two Gaussian peaks and a baseline function using Origin (OriginLab Corp., Northampton, MA). The baseline function, which is essentially the linear integral of the pristine spectrum, was used to estimate the charge-sharing effect in the energy window that is overlapped with the fluorescence signal. The recorded k_α and k_β signals were assumed to have a Gaussian distribution with similar peak width.[17,27] Since the charge-sharing fractions were assumed to be independent of incoming photon flux, the ratio between k_α and k_β peak areas should remain the same as the theoretical values. This assumption was implemented in the fitting as an additional constrain. The center (μ) and the full-width-at-half-maximum (FWHM) of the fitted peaks were recorded for each fluorescence peaks from all four target materials. To calibrate the measured pulse height to the incident photon energy, the fitted peak centers (t_c) were plotted as a function of the known fluorescence energies, and fitted with the following linear function:

$$t_c = gE + \mu_0, \quad (2)$$

where g and μ_0 are the averaged gain and offset values for all detector pixels, which can then be used to convert measured pulse height in unit of mV to the actual photon energy in keV.

2.C.2. Detector energy resolution

The energy resolution of the detector was derived from the FWHM of the fitted Gaussian peaks. The FWHMs were assumed to be approximately the same for k_α and k_β peaks, due to the small energy difference between the two. This constraint was necessary for low Z targets, where k_α and k_β overlapped significantly, and reduced the arbitrariness during peak fitting. For high Z targets, where k_α and k_β can be well resolved, such constraint was satisfied automatically from the optimal fitting. Finally, the relative energy resolution of the detector R_E for a given target with fluorescence at energy E was determined as

$$R_E = \frac{\mathrm{FWHM}}{gE}, \quad (3)$$

where g is the gain factor determined from Eq. (2), and FWHM was measured in unit of mV.

2.C.3. Charge-sharing fractions

Charge-sharing contributes to the low energy tails recorded in the pulse height distribution (Fig. 3). In general, the signal induced by charge-sharing can be fitted with a constant baseline in regions outside the primary fluorescence peaks.[17,27] Within the fluorescence region, the charge-sharing signal was estimated from the linear integral of the fluorescence. The investigated Si strip detector consists of a single line of pixels

with a 100 μm pitch. The probability of a detected photon being shared by more than two pixels is very small, as the estimated photoelectron range and the charge diffusion are both less than 50 μm.[7] Therefore, in case of charge-sharing, the absorbed x-ray photon generally produces a primary and a secondary detected count. The energy shared by the secondary count will be limited to the half of the incoming photon energy $(E/2)$.[27] The charge-sharing fraction (η), which is defined as the ratio between the number of photons that experienced a charge-sharing process and the total detectible photons, can be calculated as

$$\eta = \frac{N_c + N_e}{N_c + N_e + N_g}, \tag{4}$$

where N_c is the integrated signal between $E/2$ and the onset of the fluorescence peaks. N_e is the integrated signal of the baseline function (solid red line in Fig. 3) used to estimate the charge-sharing in the fluorescence region. N_g is the integrated signal of the Gaussian peaks (green dashed and blue dotted lines in Fig. 3) used to fit k_α and k_β fluorescence.

2.C.4. Detector's energy response function

In order to model the detector's energy response function over the entire dynamic range, the measured energy resolutions and charge-sharing fractions from the four fluorescent targets were interpolated between 10 and 70 keV. In order to handle the nonlinearity of the measured data, second order polynomial functions were used to estimate the energy dependence of the energy resolutions $R(E)$ and the charge-sharing fraction $\eta(E)$ through least squares fitting of calibration data from the four fluorescent targets. This approach allows for the estimation of the energy resolution and the charge-sharing fraction for any given energy E, which was used in the following calculation of the detector's energy response function.

In this study, a semianalytical model with four parameters $[\sigma(E), C_1(E), C_2(E), \text{and } C_3(E)]$ will be used to describe the detector's energy response function. To simplify the mathematical expressions, we will only give the analytical format of the detector response function in energy domain $[\mathrm{DRF}(\mu, E)]$, where μ and E are the measured and incident photon energies, respectively. The detector's energy response function $\mathrm{DRF}(t, E)$ in the pulse height domain, where t represents the actual pulse height in mV, can be easily correlated to $\mathrm{DRF}(\mu, E)$ through the pulse height calibration shown in Eq. (2). Due to the absence of the fluorescence escape from Si, the model only includes a primary fluorescence peak, a complementary error function baseline, and a constant baseline. The model can be expressed as the following piecewise function:

$$\mathrm{DRF}(\mu, E) = \begin{cases} C_1(E) & for\ E/2 < \mu < E - 3\sigma \\ \dfrac{C_2(E)}{\sqrt{2\pi}\sigma(E)} \exp\left(-\dfrac{(\mu - E)^2}{2\sigma(E)^2}\right) + \dfrac{2C_3(E)}{\sqrt{2\pi}\sigma(E)} \displaystyle\int_\mu^\infty \exp\left(-\frac{(\mu - E)^2}{2\sigma(E)^2}\right) d\mu & for\ \mu > E - 3\sigma \end{cases}, \tag{5}$$

where $\sigma(E)$ is the standard deviation of the primary Gaussian peak, and was determined by

$$\sigma(E) = \frac{\mathrm{FWHM}}{2\sqrt{2\ln 2}} = \frac{E}{2\sqrt{2\ln 2}} R(E), \tag{6}$$

where all values have been converted into energy domain with unit of keV. The other three fitting parameters $[C_1(E), C_2(E), \text{and } C_3(E)]$ determine the amplitude of the corresponding functions, which are related to the fitted charge-sharing fractions and were estimated through the following three constrains:

$$\eta(E) = \frac{C_1(E) * \left(\frac{E}{2} - 3\sigma(E)\right) + C_3(E) * \int \mathrm{erfc}(\mu)}{C_1(E) * \left(\frac{E}{2} - 3\sigma(E)\right) + C_3(E) * \int \mathrm{erfc}(\mu) + C_2(E)}, \tag{7}$$

$$C_1(E) = C_2(E) * \mathrm{Gaussian}(E - 3\sigma) + C_3(E) * \mathrm{erfc}(E - 3\sigma), \tag{8}$$

$$C_1(E) * \left(\frac{E}{2} - 3\sigma(E)\right) + C_3(E) * \int \mathrm{erfc}(\mu) + C_2(E) = I_d(E) = I_0(E) e^{-\mu_{Si} t}. \tag{9}$$

Equation (7) is derived from the definition of charge-sharing fraction as discussed in Sec. 2.C.3, where the total integrated areas of the constant baseline and the error functions were divided by the sum of all signals. Equation (8) applies a boundary condition so that the proposed piecewise response function was continuous at the tail of the fluorescence peak $(E - 3\sigma)$. Finally, Eq. (9) defines the total signal to be the number of detected photons, which can be derived from the input spectrum $[I_0(E)]$, the linear attenuation coefficient of Si (μ_{Si}), and the detector thickness (t). It should be noted here that charge-sharing induced double counts were not included in Eq. (9), as we only include signal above $E/2$. Upon determining all four parameters, the detector response can be predicted for incident photons with any given energy. By summing the detector response over the full energy range, an ideal incident x-ray spectrum can be converted to a more realistic spectrum that is produced by the detector.

3. RESULTS

The pulse height distribution obtained from the fluorescence calibrations of Ag, I, Ba, and Gd, along with that of $CaCO_3$, are shown in Fig. 4. All spectra were acquired at 100 kVp and 4 mA, with a 7.5 s detector frame time. Strong

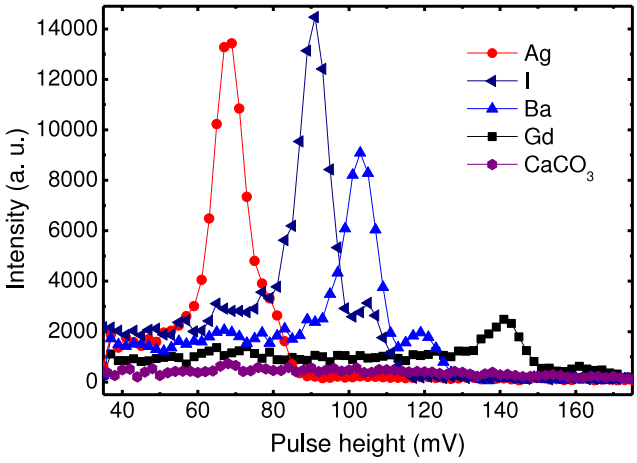

FIG. 4. The recorded fluorescence spectra from Ag, I, Ba, and Gd acquired at the same tube output. The spectrum measured with $CaCO_3$ is also shown, which is used to estimate the background scatter.

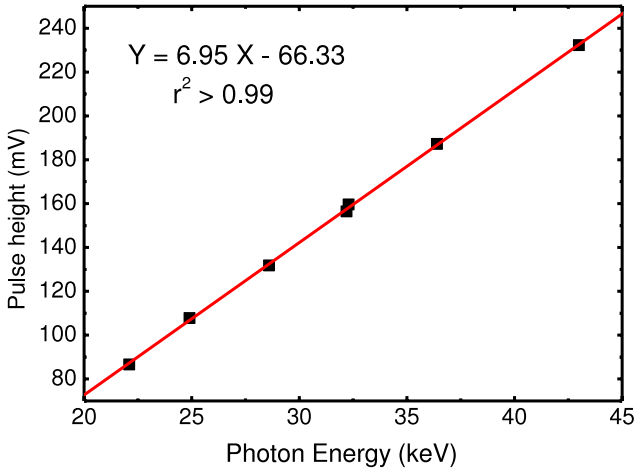

FIG. 5. Linear correlation between the recorded pulse heights at the peak centers and the known fluorescence photon energies. Gain and offset values for the detector energy calibration were determined to be 6.95 mV/keV and −66.33 mV, respectively.

signals can be observed at the discriminator voltages that correspond to the fluorescence energies of the four target materials. Both k_α and k_β peaks can be identified in the fluorescence measurement, although they were not fully resolved in the case of Ag due to the small energy separation between the two peaks. The shape of the peaks can be well described by Gaussian functions. The main fluorescence peaks showed a slight asymmetry in all cases. More importantly, a rather constant background can be found in the low energy side of the fluorescence peak, which extended down to the noise floor. As discussed in Sec. 2.C.3, the slight asymmetry of the fluorescence peak, as well as the constant background below the fluorescence energy can be attributed to charge-sharing events. For energies above the fluorescence peaks, there was hardly any signal, which suggested the absence of pulse pileup under the investigated photon flux. The maximum count rate in the raw data, which is the integral of the fluorescence spectra, was found to be approximately 0.8 Mcps/mm^2, which is well within the linear counting range of the investigated Si strip detector.[39] The recorded fluorescence intensities from the four target materials varied significantly. This variation can be attributed to the differences in the number of photons available to excite the k-shell electron, the physical concentrations of the fluorescent atoms in the target phantoms, and the quantum efficiency of the Si strip detector at different energies. The spectrum recorded for $CaCO_3$ is also presented, which measured the scatter signal from the target. The scatter intensity was found to be several orders of magnitude less than the intensity of the fluorescence. This difference in intensity can be explained by the small target size and the detector collection angle.

By applying the data fitting process discussed in Sec. 2, the peak center of k_α and k_β fluorescence for all four materials was obtained and plotted as a function of the known fluorescence energies in Fig. 5. Linear regression analysis was performed to calibration the recorded pulse height to the incident photon energy. An excellent linear energy response was found for the Si strip detector within the investigated energy range. According to Eq. (2), the gain and offset were determined to be 6.95 mV/keV and −66.33 mV. The measured correlation relates the output of a photon-counting detector to the actual photon energy, which provides the foundation for spectral imaging.

In imaging mode, a universal threshold will be used across all detector pixels. It is thus interesting to study the pixel variations in terms of energy response. As an example, the k_α fluorescence photon peak of iodine was measured for each of the 256 pixels in the detector, and presented as a function of pixel index in Fig. 6(a). The peak centers were calibrated based on Eq. (2), so that the mean value of all pixels equals the k_α fluorescence energy of 28.6 keV. Pixel variation was observed with a standard deviation of approximately 0.5 keV. This deviation is due to the accuracy with which the initial offset corrections to each threshold can be applied. The minimum and maximum values were found to be 27.4 and 29.7 keV. In addition, the consistency of the four thresholds that were available with the investigated detectors was also investigated with iodine fluorescence signal. The fluorescence spectra obtained by scanning the four thresholds together are shown in Fig. 6(b). It can be observed that the variation induced by thresholds can be neglected.

The measured FWHM of the fluorescence peaks and the percent energy resolution is shown in Figs. 7(a) and 7(b), respectively. Following the general application, the FWHM was converted into the energy domain with a unit of keV by using the gain factor determined in Fig. 5. It can be seen that the absolute FWHM remained relatively stable at approximately 2.7 keV for energy range between 20 and 35 keV. This result is in good agreement with the previous measurement on the same detector using ^{109}Cd isotopes.[39] For high energy photons at 46 keV, the FWHM increased slightly to 3.2 keV. Such broadening may be attributed to the dominance of Compton scatter over photoelectric effect at this energy. However, by normalizing with respect to the corresponding fluorescence energies, the percent energy resolution actually decreased as a function of energy. The calibration data

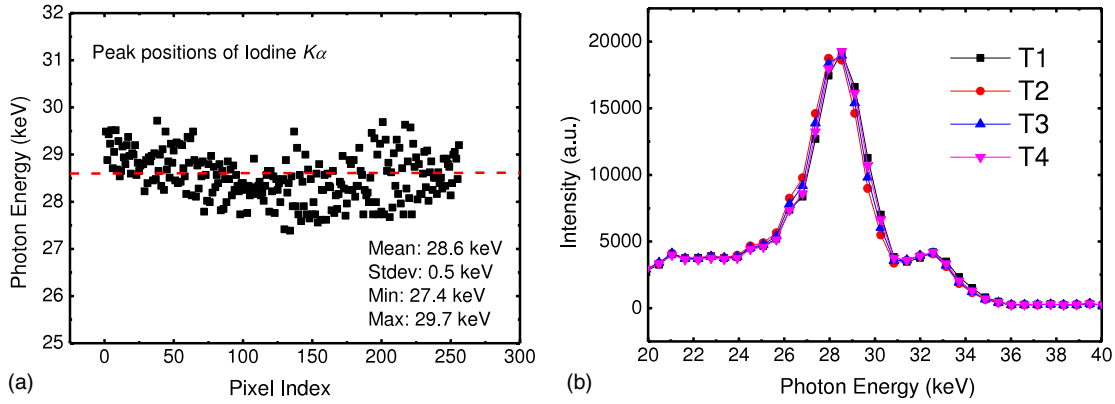

FIG. 6. (a) The calibrated iodine k_α energies measured for each of the 256 pixels on the Si strip detector. (b) The calibrated iodine fluorescence spectra measured with the four voltage discriminators of the detector.

were fitted with a polynomial function as shown in the solid line in Fig. 7(b). The obtained analytical fitting function was then used to predict the standard deviation of the Gaussian function used in the detector response function according to Eq. (6) for any given energy.

Figure 8 shows the measured charge-sharing fractions for the four fluorescence energies. The fraction of charge-shared events was estimated to be approximately 20%–30% for photon energies less than 30 keV. These numbers are larger than the values reported recently on a Si strip detector.[27] However, the investigated detector in Ref. 27 has a pixel strip width size of 0.4 mm, while our detector strip width size was 0.1 mm. The increased charge-sharing fractions can be attributed to the smaller pixel pitch used in this study. The calibration result also suggested that the charge-sharing fraction increased at high energy. Above 40 keV, over half of the detected photons may experience a charge-sharing event. This is mostly caused by the significant increase of the Compton scattering cross section for photons at those energies. The averaged charge-sharing fraction over the investigated energy range was approximately 36%. Similar to the process used in energy resolution analysis, the four calibration points here were used to derive the charge-sharing fraction as a function of energy using polynomial fitting. The resulting analytical function was used to determine the parameters $[C_1(E), C_2(E),$ and $C_3(E)]$ in the detector response function according to Eqs. (7)–(9).

Based on the fittings of the energy resolution and charge-sharing fraction data, the detector's energy response function was calculated for any given energy between 10 and 65 kVp. To validate this method, the detector response function at 32 keV obtained by analytical modeling using Eq. (6) was compared to the experimental data from Ba, whose k_α fluorescence can be found at 32.2 keV. The result is shown in Fig. 9. It should be noted that the solid line was not a direct fitting of the experimental data; it was obtained from analytical calculations. It can be observed that the analytical model of the detector response function agreed well with the experimental data, in terms of fluorescence peak intensity, width, and low energy background. Since the detector's energy response function shown here was derived only for photons at 32 keV, the k_β fluorescence of Ba was not included, which explains the small difference at the low energy tail of the fluorescence peak. Finally, the detector output from a polyenergetic incident x-ray spectrum at 65 kVp with 2.7 mm Al filter was simulated using the proposed detector's energy response function. The comparison between the simulated output spectrum and the experimental measurement is presented in Fig. 10. The incident x-ray spectrum was obtained using TASMIP code, which was developed based on

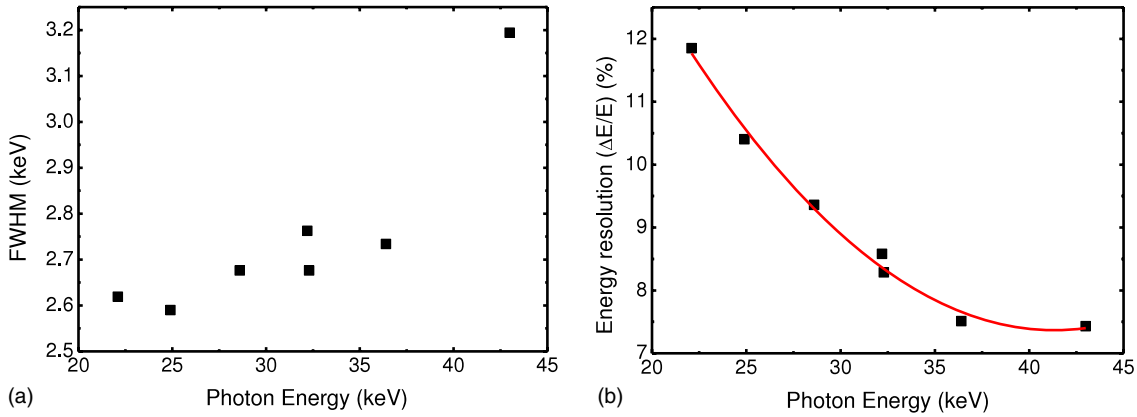

FIG. 7. The FWHM (a) and the percent energy resolutions (b) obtained by analytical fitting of the recorded fluorescence spectra from Ag, I, Ba, and Gd. A polynomial fitting was used to interpolate the energy resolution for any given photon energy.

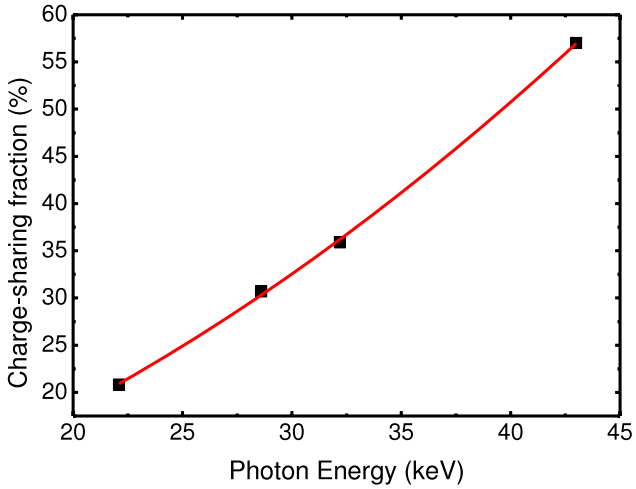

FIG. 8. Charge-sharing fractions obtained by analytical fitting of the recorded fluorescence spectra from Ag, I, Ba, and Gd. A polynomial fitting was used to interpolate the charge-sharing fraction for any given photon energy.

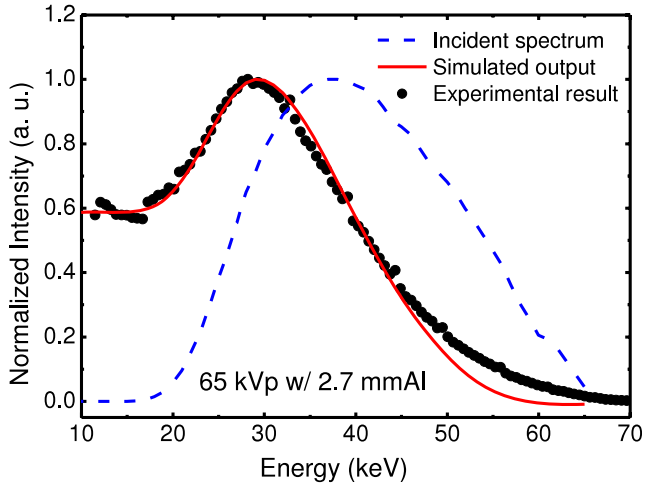

FIG. 10. Comparison between the simulation using the analytical modeling of the detector response function and the experimental measurement of a 65 kVp spectrum. The ideal incident spectrum simulated by TASMIP code is also shown.

previous Monte Carlo simulation.[40] The simulated detector response function was applied on the incident spectrum for each keV, and summed together to produce the simulated detector output. The intensities of the measured and simulated spectra were normalized. In general, we found a good agreement between the two spectra, especially in the low energy region. It has been previous reported that photon-counting detectors measured significantly higher count at low energies, in comparison to the theoretical x-ray spectrum.[7,30] Our analytical model for the detector response function successfully predicted this behavior using the calibration data from x-ray fluorescence measurements. One may also notice some discrepancies in the measured and simulated spectra for energies above 45 keV. These discrepancies are attributed to the limitation of our calibration energy range. This issue can be addressed by using fluorescence targets with higher energies, which will improve the fitting accuracy. However, in this study, the signal intensity above 45 keV was substantially low in the incident spectrum. This is not only because of the photon energy distribution in a bremsstrahlung radiation spectrum but also because of the low detector quantum efficiency at high energies. Therefore, the errors in the estimation of the detector response function at such energies may not contribute significantly to the overall simulation of the detector output.

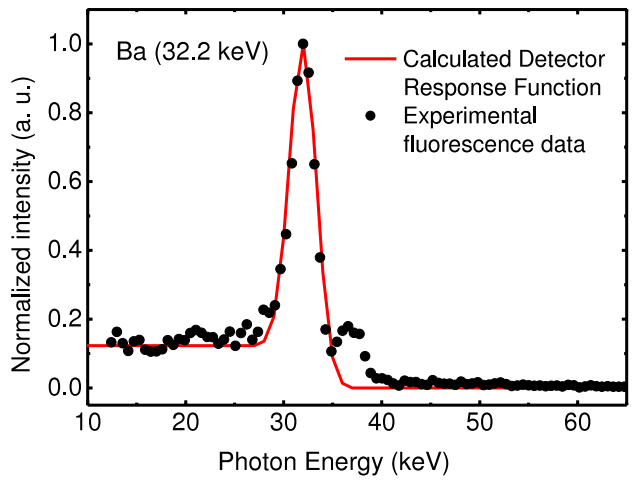

FIG. 9. Comparison between the analytical modeling of the detector response function at 32 keV and the experimental measurement from Ba whose fluorescence is at 32.2 keV. The proposed analytical model accurately predicted the detector output with a monoenergetic input.

4. DISCUSSION

Owing to their unique abilities to count individual photons with the spectral information at high flux, photon-counting detectors of this type offer a promising future for spectral x-ray imaging. At the same time, in order to take advantage of the spectral information, the development of an accurate energy response function is required with additional quality control processes that are not routinely performed for conventional charge-integrating detector. Since the photon-counting detectors convert interacted photon energy into electronic pulses, a good understanding about the detector response, in terms of pulse height calibration and energy resolution, is crucial to evaluate and predict the performance of the detector in realistic applications. In this study, we investigated an easily adapted method to characterize a Si strip photon-counting detector by using x-ray fluorescence calibrations. The fluorescence from various target materials was used as quasi-monoenergetic photon sources to investigate the detector response. The energy calibration was accomplished by measuring the peak center of the recorded fluorescence spectra. The energy resolution was obtained from the width of the fluorescence peak. A good accuracy was achieved within a short acquisition time of a few minutes. Although a small FOV line detector was used in this study, the experimental setup for the fluorescence measurement can be potentially used to calibrate detectors of large FOV. The proposed method can be readily implemented in standard imaging laboratories

to calibrate the detector's energy response, so that reliable energy information can be obtained for spectral imaging. This method simultaneously measures the energy response for each detector pixel. Pixel-based response functions can be derived, given sufficient counting statistics. Thus, it can be used to fine tune the voltage comparators associated with each pixel, so that the pixel variation can be minimized. Finally, the fluorescence calibration, as well as the proposed analytical fitting, provides a way to model the detector response function for a broad energy range that is relevant to diagnostic imaging. The analytical model can be used in simulation studies to better predict the detector output.[17] It is thus valuable in many applications, such as material decomposition, imaging protocol optimization, and image quality comparisons between different detectors.

As an initial feasibility study, four fluorescent targets, Ag, I, Ba, and Gd, were used in this study. The selection of these target materials was based on their fluorescence energies, as well as common availability in a medical imaging laboratory. In theory, any stable compound, which is consisted of elements with atomic number larger than 30, will produce k-fluorescence above 10 keV,[41] and may be used for fluorescence calibration. One limitation of this study is the lack of calibration points at energies above 43 keV. As discussed in Sec. 3, the fitting errors induced by the lack of high energy calibration points are expected to be small in this study. Nevertheless, this issue can be addressed by employing more fluorescent materials in the calibration. An ideal selection of the calibration points may include multiple targets whose fluorescence energies are separated by approximately 10 keV. Using the proposed method, the detector energy response can be calibrated up to 100 keV,[41] which is close to the energy range for diagnostic imaging. With adequate calibration points, the fitting function used for energy resolution and charge-sharing can be further optimized. For example, a piecewise linear function may provide a good estimation for these tasks.[17]

The investigated Si strip detector employs a small pixel pitch and fast readout ASICs. The detector count rate is linear to 40 Mcps/mm^2 and saturates just below 100 Mcps/mm^2.[39] Therefore, spectral distortion induced by pulse pileup is expected to be negligible. In the initial test, iodine fluorescence spectra were measured at various tube voltages ranging from 70 to 120 kVp (result not shown). No discernible signal was observed at energies above the fluorescence peaks. In addition, the widths of the fluorescence peaks remain intact when varying the incoming photon flux. These observations suggested that the energy resolution did not deteriorate under the investigated photon flux. However, substantial pixel variation was observed as shown in Fig. 6(a). This is mostly due to the "global" calibration used in this study and would be mostly eliminated with a pixel by pixel calibration. Since the energy resolution was derived from the total signal of all pixels, it is unavoidably affected by the pixel variations. FWHM derived from a single pixel, which can also be obtained with the current study, will be substantially smaller than the results shown in Fig. 7. However, pixel by pixel calibration using an individual trim DAC for each threshold can be very time consuming and is out of the scope of this study.

In the proposed fluorescence calibration setup, a right angle between the detector and incident beam was used to collect the fluorescence photons. This setup is designed primarily to take in the consideration to minimize scatter from the target. According to the Klein–Nishina formula, the Compton scattering cross section is minimized at 90° for the investigated photon energies. However, by varying the angle between the x-ray source and the detector, we found that the fluorescence-to-scatter ratio increased toward the backscattering direction. This phenomenon can be attributed to the attenuation of the target, which produced more fluorescence photons at the back angle. Further studies about the optimal experimental setup and the angular dependence are currently under investigation. Unfortunately, the back angle acquisition in this study was limited by the physical size of the x-ray source and the Si strip detector. Such measurement can only be carried out at increased target to detector distance, which dramatically reduced the fluorescence photon flux at the detector.

The conventional methods to calibrate a photon-counting detector generally rely on monoenergetic photon beams produced by synchrotron radiation or radioactive isotopes. Both of the two photon sources require specific facilities and are difficult to implement in an imaging laboratory as a routine calibration procedure. Another commonly used method calibrates the high energy onset of the recorded spectra with respect to the maximum tube voltage (kVp) used. This technique is easy to implement, however, it does require an x-ray source whose tube voltage can be adjusted in a fairly wide range. Comparing to the proposed fluorescence calibration method, the maximum kVp technique is more susceptible to the detector's spectral distortions. For example, the presence of pulse pileup may affect the measurement of the high energy onset in the recorded spectrum. In addition, the measurement of the maximum kVp is performed at the part of spectrum where the recorded count is close to zero, while the fluorescence calibration always measures at the part of the spectrum where the count is maximized. From a statistical point of view, fluorescence calibration is affected less by the noise in the recorded spectra, leading to higher reproducibility and smaller inter- and intro-observer variations than those of the maximum kVp technique. More importantly, the maximum kVp technique can only be used for simple pulse height calibrations and is inadequate for the energy resolution and detection response calibrations.

The main limitation of fluorescence calibration is that the incident photon beam is not monoenergetic, which also include scattered photons from the target. However, using a small target size and proper experimental setup, the background scatter signal can be effectively minimized. Further, the scatter can be estimated using low Z materials, and subtracted from the recorded fluorescence spectra. In this study, we estimated the background scatter with $CaCO_3$, whose spectrum intensity was at least one order of magnitude less than that of the fluorescent targets for any given photon energy. Therefore, uncertainties in background scatter estimation may not have a significant

contribution to the subsequent fluorescence calibrations. The use of $CaCO_3$ was also evaluated using an x-ray spectrometer (XR-100T, Amptek, Inc., Bedford, MA), which is free of charge-sharing since it has only one detector pixel. The spectrometer measurements suggested that the recorded spectra from $CaCO_3$ and iodine agreed very well at energies below the fluorescence peaks, which justified the use of $CaCO_3$ in this study.

Characteristic x-ray escape is not an issue for Si strip detectors, due to its low atomic number. However, for detectors with high Z elements, such as CdTe, the presence of characteristic x-ray escape may significantly modify the detector response function. Characteristic x-rays can be emitted when the incident photon energy is above the k-edge energy of Cd or Te. To implement the proposed fluorescence calibration technique, an additional set of Gaussian peaks should be used at the energy reduced by the corresponding k-edge energy.[42] Furthermore, in some applications, such as breast imaging, where low energy photons can also contribute to the recorded signal, the reabsorption of the escaped characteristic photon will also need to be considered.[43] The average k-shell characteristic x-ray energy emitted from Cd and Te are 23.4 and 27.5 keV, respectively. A set of Gaussian peaks can be used to fit the reabsorption process at these energies.

5. CONCLUSION

In conclusion, we investigated an easily adapted technique to characterize a Si strip detector using x-ray fluorescence calibrations. The technique utilized the k-shell fluorescence from Ag, I, Ba, and Gd to calibrate the detector pulse height with respect to the known fluorescence energies. The gain and offset were determined to be 6.95 mV/keV and −66.33 mV, respectively. The energy resolutions and charge-sharing fractions were also obtained from analytical fittings of the recorded fluorescence spectra. An analytical model, which employed four parameters that can be determined from the fluorescence calibration, was used to estimate the detector response function. The simulated detector output based on the proposed response function was in good agreement with the experimental measurement. The result of the study suggested that the proposed fluorescence calibration technique can be readily implemented in a standard imaging laboratory to calibrate the energy response of a photon-counting detector.

ACKNOWLEDGMENTS

This work was supported in part by NIH/NCI Grant Nos. R01CA13687 and R44CA177093.

[a]Author to whom correspondence should be addressed. Electronic mail: symolloi@uci.edu; Telephone: (949) 824-5904; Fax: (949) 824-8115.

[1]H. Bornefalk and M. Danielsson, "Photon-counting spectral computed tomography using silicon strip detectors: A feasibility study," Phys. Med. Biol. **55**, 1999–2022 (2010).
[2]P. M. Shikhaliev and S. G. Fritz, "Photon counting spectral CT versus conventional CT: Comparative evaluation for breast imaging application," Phys. Med. Biol. **56**, 1905–1930 (2011).
[3]D. P. Cormode, E. Roessl, A. Thran, T. Skajaa, R. E. Gordon, J. P. Schlomka, V. Fuster, E. A. Fisher, W. J. M. Mulder, R. Proksa, and Z. A. Fayad, "Atherosclerotic plaque composition: Analysis with multicolor CT and targeted gold nanoparticles," Radiology **256**, 774–782 (2010).
[4]P. M. Fralliciardi, J. Jakubek, D. Vavrik, and J. Dammer, "Comparison of single-photon counting and charge-integrating detectors for x-ray high-resolution imaging of small biological objects," Nucl. Instrum. Methods Phys. Res., Sect. A **607**, 221–222 (2009).
[5]K. Taguchi, S. Srivastava, H. Kudo, and W. C. Barber, "Enabling photon counting clinical x-ray CT," in *IEEE Nuclear Science Symposium and Medical Imaging Conference (NSS/MIC 2009)* (IEEE, Orlando, FL, 2009).
[6]K. S. Kalluri, M. Mahd, and S. J. Glick, "Investigation of energy weighting using an energy discriminating photon counting detector for breast CT," Med. Phys. **40**, 081923 (16pp.) (2013).
[7]X. Wang, D. Meier, S. Mikkelsen, G. E. Maehlum, D. J. Wagenaar, B. M. W. Tsui, B. E. Patt, and E. C. Frey, "MicroCT with energy-resolved photon-counting detectors," Phys. Med. Biol. **56**, 2791–2816 (2011).
[8]H. Ding, J. L. Ducote, and S. Molloi, "Breast composition measurement with a cadmium-zinc-telluride based spectral computed tomography system," Med. Phys. **39**, 1289–1297 (2012).
[9]G. K. Yadava, A. T. Kuhls-Gilcrist, S. Rudin, V. K. Patel, K. R. Hoffmann, and D. R. Bednarek, "A practical exposure-equivalent metric for instrumentation noise in x-ray imaging systems," Phys. Med. Biol. **53**, 5107–5121 (2008).
[10]K. Kalluri, S. J. Glick, and M. Mahd, "SNR improvement in dedicated breast CT using energy weighting with photon counting detectors," in *37th Annual Northeast Bioengineering Conference (NEBEC 2011)* (IEEE, Troy, NY, 2011), pp. 1–2.
[11]H. Bornefalk, "Task-based weights for photon counting spectral x-ray imaging," Med. Phys. **38**, 6065–6073 (2011).
[12]T. G. Schmidt, "Optimal 'image-based' weighting for energy-resolved CT," Med. Phys. **36**, 3018–3027 (2009).
[13]H. Q. Le, J. L. Ducote, and S. Molloi, "Radiation dose reduction using a CdZnTe-based computed tomography system: Comparison to flat-panel detectors," Med. Phys. **37**, 1225–1236 (2010).
[14]N. A. G. Giersch, "The influence of energy weighting on x-ray imaging quality," Nucl. Instrum. Methods Phys. Res., Sect. A **531**, 68–74 (2004).
[15]H. Q. Le and S. Molloi, "Segmentation and quantification of materials with energy discriminating computed tomography: A phantom study," Med. Phys. **38**, 228–237 (2011).
[16]H. Q. Le and S. Molloi, "Least squares parameter estimation methods for material decomposition with energy discriminating detectors," Med. Phys. **38**, 245–255 (2011).
[17]E. Roessl and R. Proksa, "K-edge imaging in x-ray computed tomography using multi-bin photon counting detectors," Phys. Med. Biol. **52**, 4679–4696 (2007).
[18]C. Bert, D. Niederlohner, J. Giersch, K. F. Pfeiffer, and G. Anton, "Computed tomography using the Medipix1 chip," Nucl. Instrum. Methods Phys. Res., Sect. A **509**, 240–250 (2003).
[19]M. G. Bisogni, A. Del Guerra, N. Lanconelli, A. Lauria, G. Mettivier, M. C. Montesi, D. Panetta, R. Pani, M. G. Quattrocchi, P. Randaccio, V. Rosso, and P. Russo, "Experimental study of beam hardening artifacts in photon counting breast computed tomography," Nucl. Instrum. Methods Phys. Res., Sect. A **581**, 94–98 (2007).
[20]M. Chmeissani, C. Frojdh, O. Gal, X. Llopart, J. Ludwig, M. Maiorino, E. Manach, G. Mettivier, M. C. Montesi, C. Ponchut, P. Russo, L. Tlustos, and A. Zwerger, "First experimental tests with a CdTe photon counting pixel detector hybridized with a Medipix2 readout chip," IEEE Trans. Nucl. Sci. **51**, 2379–2385 (2004).
[21]D. Niederlohner, F. Nachtrab, T. Michel, and G. Anton, "Using the Medipix2 detector for photon counting computed tomography," *Nuclear Science Symposium Conference Record* (IEEE, Wyndham EI Conquistador Resort, Puerto Rico, 2005).
[22]D. J. Wagenaar, S. Chowdhury, J. C. Engdahl, and D. D. Burckhardt, "Planar image quality comparison between a CdZnTe prototype and a standard NaI(T1) gamma camera," Nucl. Instrum. Methods Phys. Res., Sect. A **505**, 586–589 (2003).
[23]W. C. Barber, E. Nygard, J. S. Iwanczyk, M. Zhang, E. C. Frey, B. Tsui, J. C. Wessel, N. Malakhov, G. Wawrzyniak, N. E. Hartsough, T. Gandhi, and K. Taguchi, "Characterization of a novel photon counting detector for

clinical CT: Count rate, energy resolution, and noise performance," Proc. SPIE **7258**, 725824–725829 (2009).
[24]D. Pan, E. Roessl, J. P. Schlomka, S. D. Caruthers, A. Senpan, M. J. Scott, J. S. Allen, H. Y. Zhang, G. Hu, P. J. Gaffney, E. T. Choi, V. Rasche, S. A. Wickline, R. Proksa, and G. M. Lanza, "Computed tomography in color: NanoK-enhanced spectral CT molecular imaging," Angew. Chem., Int. Ed. **49**, 9635–9639 (2010).
[25]H. Toyokawa, Y. Furukawa, T. Hirono, H. Ikeda, K. Kajiwara, M. Kawase, T. Ohata, G. Sato, M. Sato, T. Takahashi, H. Tanida, T. Uruga, and S. Watanabe, "Si and CdTe pixel detector developments at SPring-8," Nucl. Instrum. Methods Phys. Res., Sect. A **636**, S218–S221 (2011).
[26]T. Takahashi and S. Watanabe, "Recent progress in CdTe and CdZnTe detectors," IEEE Trans. Nucl. Sci. **48**, 950–959 (2001).
[27]C. Xu, H. Chen, M. Persson, S. Karlsson, M. Danielsson, C. Svensson, and H. Bornefalk, "Energy resolution of a segmented silicon strip detector for photon-counting spectral CT," Nucl. Instrum. Methods Phys. Res., Sect. A **715**, 11–17 (2013).
[28]E. Guni, J. Durst, B. Kreisler, T. Michel, G. Anton, M. Fiederle, A. Fauler, and A. Zwerger, "The influence of pixel pitch and electrode pad size on the spectroscopic performance of a photon counting pixel detector with CdTe sensor," IEEE Trans. Nucl. Sci. **58**, 17–25 (2011).
[29]R. Aamir, S. P. Lansley, R. Zainon, M. Fiederle, A. Fauler, D. Greiffenberg, P. H. Butler, and A. P. H. Butler, "Pixel sensitivity variations in a CdTe-Medipix2 detector using poly-energetic x-rays," J. Instrum. **6**, C01059 (2011).
[30]H. Ding and S. Molloi, "Image-based spectral distortion correction for photon-counting x-ray detectors," Med. Phys. **39**, 1864–1876 (2012).
[31]A. S. Wang, D. Harrison, V. Lobastov, and J. E. Tkaczyk, "Pulse pileup statistics for energy discriminating photon counting x-ray detectors," Med. Phys. **38**, 4265–4275 (2011).
[32]K. Taguchi, M. Zhang, E. C. Frey, X. Wang, J. S. Iwanczyk, E. Nygard, N. E. Hartsough, B. M. W. Tsui, and W. C. Barber, "Modeling the performance of a photon counting x-ray detector for CT: Energy response and pulse pileup effects," Med. Phys. **38**, 1089–1102 (2011).
[33]R. Ballabriga, G. Blaj, M. Campbell, M. Fiederle, D. Greiffenberg, E. H. M. Heijne, X. Llopart, R. Plackett, S. Procz, L. Tlustos, D. Turecek, and W. Wong, "Characterization of the Medipix3 pixel readout chip," J. Instrum. **6**, C01052 (2011).
[34]T. Campbell-Ricketts and M. Das, "Direct spectral recovery using x-ray fluorescence measurements for material decomposition applications using photon counting spectral x-ray detectors," Proc. SPIE **9033**, 90331D (2014).
[35]K. Iwata, J. M. Star-Lack, E. G. Solomon, J. A. Heanue, R. E. Walkup, and R. E. Melen, "Energy-dependent quantum detective efficiency (QDE) measurements of a photon-counting CdTe detector array used for the scanning-beam digital x-ray (SBDX) system," Proc. SPIE **5030**, 818–825 (2003).
[36]J. Jakubek, "Precise energy calibration of pixel detector working in time-over-threshold mode," Nucl. Instrum. Methods Phys. Res., Sect. A **633**, S262–S266 (2011).
[37]J. P. Ronaldson, M. Walsh, S. J. Nik, J. Donaldson, R. M. N. Doesburg, D. van Leeuwen, R. Ballabriga, M. N. Clyne, A. P. H. Butler, and P. H. Butler, "Characterization of Medipix3 with the MARS readout and software," J. Instrum. **6**, C01056 (2011).
[38]M. Aslund, B. Cederstrom, M. Lundqvist, and M. Danielsson, "Physical characterization of a scanning photon counting digital mammography system based on Si-strip detectors," Med. Phys. **34**, 1918–1925 (2007).
[39]H.-M. Cho, W. C. Barber, H. Ding, J. S. Iwanczyk, and S. Molloi, "Characteristic performance evaluation of a photon counting Si strip detector for low dose spectral breast CT imaging," Med. Phys. **41**, 091903 (10pp.) (2014).
[40]J. M. Boone and J. A. Seibert, "Accurate method for computer-generating tungsten anode x-ray spectra from 30 to 140 kV," Med. Phys. **24**, 1661–1670 (1997).
[41]T. Schoonjans, A. Brunetti, B. Golosio, M. S. del Rio, V. A. Sole, C. Ferrero, and L. Vincze, "The xraylib library for x-ray-matter interactions. Recent developments," Spectrochim. Acta, Part B **66**, 776–784 (2011).
[42]J. P. Schlomka, E. Roessl, R. Dorscheid, S. Dill, G. Martens, T. Istel, C. Baumer, C. Herrmann, R. Steadman, G. Zeitler, A. Livne, and R. Proksa, "Experimental feasibility of multi-energy photon-counting k-edge imaging in pre-clinical computed tomography," Phys. Med. Biol. **53**, 4031–4047 (2008).
[43]S. J. Glick and C. Didier, "Investigating the effect of characteristic x-rays in cadmium zinc telluride detectors under breast computerized tomography operating conditions," J. Appl. Phys. **114**, 144506 (2013).